

# Spinel manganese oxide: A high capacity positive electrode material for the sodium ion battery



Riki Kataoka, Mitsunori Kitta, Hiroyuki Ozaki, Nobuhiko Takeichi, Tetsu Kiyobayashi\*

Research Institute of Electrochemical Energy, Department of Energy and Environment, National Institute of Advanced Industrial Science and Technology (AIST), 1-8-31 Midorigaoka, Ikeda, Osaka 563-8577, Japan

## ARTICLE INFO

### Article history:

Received 11 April 2016

Received in revised form 8 June 2016

Accepted 7 July 2016

Available online 11 July 2016

### Keywords:

Sodium ion battery

Spinel structure

Manganese-based material

Electrode performance

Structural analysis

## ABSTRACT

This is the first report about a spinel manganese oxide that serves as a high capacity positive electrode material for the sodium ion battery. By electrochemically extracting Li from a monoclinic layered  $\text{Li}_2\text{MnO}_3$ , we prepared  $\text{Li}_{2-x}\text{MnO}_3$  ( $x = 1.6\text{--}1.8$ ) of which the Li-extracted domain has a cubic spinel structure. The reversible discharge and charge capacity of  $\text{Li}_{2-x}\text{MnO}_3$  versus the Na negative electrode initially exceeded  $200 \text{ mA} \cdot \text{h} \cdot \text{g}^{-1}$ , suggesting that close to one molar equivalent of Na is inserted in and extracted from the formula unit,  $\text{Li}_{2-x}\text{MnO}_3$ . The electrode retains the capacity of  $160 \text{ mA} \cdot \text{h} \cdot \text{g}^{-1}$  after 50 cycles. On the other hand, the  $\text{Li}_{2-x}\text{MnO}_3$  electrode versus the Li negative electrode significantly degrades upon cycling.

The *ex-situ* synchrotron X-ray diffraction (SR-XRD) and transmission electron microscopy (TEM) analyses revealed that the spinel domain of  $\text{Li}_{2-x}\text{MnO}_3$  retains its crystallographic structure during the Na insertion and extraction, although the crystal significantly loses its periodicity when Na is inserted. A numerical simulation of the SR-XRD profile suggests that the Na-inserted  $\text{Li}_{2-x}\text{MnO}_3$  has the periodicity of only one to two unit cells while retaining the spinel structure. XAS revealed that the reversible capacity is found to be dominated by the redox between Mn(III) and Mn(IV) and the Mn–Mn distance significantly loses its correlation upon Na-insertion, which is consistent with the broad SR-XRD profile.

© 2016 Elsevier Ltd. All rights reserved.

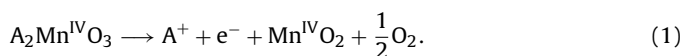
## 1. Introduction

Sodium containing Mn-based oxides have become the focus of attraction as a positive electrode material for the sodium ion battery since manganese is an abundant resource and can be considered a low-cost material [1–4]. For example,  $\alpha\text{-NaMnO}_2$  with the monoclinic structure and P2-type  $\text{Na}_{0.6}\text{MnO}_2$  with the hexagonal layered structure, have high initial reversible capacities of more than 180 and  $150 \text{ mA} \cdot \text{h} \cdot \text{g}^{-1}$ , respectively [5,6]. With the reversible capacity of only  $90 \text{ mA} \cdot \text{h} \cdot \text{g}^{-1}$  notwithstanding,  $\text{Na}_{0.44}\text{MnO}_2$  with a tunnel-type structure undergoes many cycles [7].

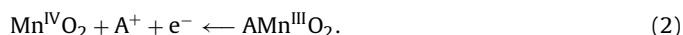
When Li is inserted in and extracted from lithium manganese oxides (e.g.,  $\text{LiMn}_2\text{O}_4$ ,  $\text{LiMnO}_2$ , etc.), the  $\text{Mn}^{3+} \rightleftharpoons \text{Mn}^{4+}$  redox is often accompanied by a crystallographic phase transition, resulting in a poor cycle stability [8]. A monoclinic layered oxide,  $\text{Li}_2\text{MnO}_3$ , is not an exception; namely, although the initial discharge capacity exceeds  $250 \text{ mA} \cdot \text{h} \cdot \text{g}^{-1}$ , the material suffers from a significant degradation upon cycling caused by the transition into a cubic

spinel structure [9]. On the other hand, the energetic barrier for such a transition is said to be much higher in the case of Na insertion and extraction [10]. If we can reversibly sodiate and desodiate  $\text{Li}_{2-x}\text{MnO}_3$  suppressing its crystallographic transition, we would be able to achieve a high capacity and long cycle-life electrode material for the sodium ion battery.

The reaction mechanism and stoichiometry of  $\text{Li}_2\text{MnO}_3$  to explain its high reversible capacity is not yet clear and still a controversy. For the discussion below, we now mention some presumable reactions, where A typically stands for Li or an alkaline metal, in general. The initial oxidation reaction is allegedly accompanied by oxygen release [11–13], which could be written as, in a complete hypothetical stoichiometry,



During the subsequent A-reinsertion, the released oxygen is considered to be hardly resumed. The following redox of Mn would be dominant:



\* Corresponding author. Tel.: +81 72 7519651; fax: +81 72 7519629.  
E-mail address: [kiyobayashi-t@aist.go.jp](mailto:kiyobayashi-t@aist.go.jp) (T. Kiyobayashi).

In the present study, we prepared  $\text{Li}_{2-x}\text{MnO}_3$  by electrochemically extracting Li from  $\text{Li}_2\text{MnO}_3$ . The electrochemical properties of  $\text{Li}_{2-x}\text{MnO}_3$  were evaluated in a half-cell setup in which Na metal was used as the counter electrode. The crystallographic structure was investigated by synchrotron X-ray diffraction (SR-XRD) and transmission electron microscope (TEM) equipped with an electron energy-loss spectrometer (EELS). The chemical state and local structure were examined by X-ray absorption spectroscopy (XAS). Broad humps in the SR-XRD profile of the sodiated  $\text{Li}_{2-x}\text{MnO}_3$  were numerically simulated to confirm its spinel structure.

## 2. Experimental Section

### 2.1. Sample preparation

A layered manganese oxide,  $\text{Li}_2\text{MnO}_3$ , as the starting material in this study was prepared by the solid-state reaction between  $\text{Li}_2\text{CO}_3$  (Kishida Chemical, purity 98%) and  $\text{Mn}_2\text{O}_3$  (Aldrich, purity 99.9%).  $\text{Li}_2\text{CO}_3$  and  $\text{Mn}_2\text{O}_3$  were mixed by ball-milling in air at the molar ratio of 2:1 for the target composition to be  $\text{Li}:\text{Mn} = 2:1$ . The mixture was calcined in a gold crucible in air for 10 h at  $800^\circ\text{C}$  at which we obtained the best qualified  $\text{Li}_2\text{MnO}_3$  sample in the examined temperature range from 400 to  $1000^\circ\text{C}$ .

The Li-extracted sample,  $\text{Li}_{2-x}\text{MnO}_3$ , was prepared by electrochemically extracting lithium from the  $\text{Li}_2\text{MnO}_3$  as follows (see the next subsection for the electrochemical cell assembly). A  $\text{Li}_2\text{MnO}_3/\text{Li}$  cell was first galvanostatically charged (*i.e.*, Li extracted or delithiated) to 4.95 V vs.  $\text{Li}^+/\text{Li}$  at the current density of  $10 \text{ mA} \cdot \text{g}^{-1}$ , then potentiostatically charged until the total amount of the charge reached  $460 \text{ mA} \cdot \text{h} \cdot \text{g}^{-1}$ . The  $\text{Li}_{2-x}\text{MnO}_3$  electrode, removed from the cell, was rinsed several times with dimethyl carbonate and then reassembled into a  $\text{Li}_{2-x}\text{MnO}_3/\text{Na}$  cell. The cell was galvanostatically discharged (*i.e.*, Na inserted or sodiated) to 1.5 V vs.  $\text{Na}^+/\text{Na}$  at the current density of  $10 \text{ mA} \cdot \text{g}^{-1}$ .

### 2.2. Electrochemical properties

The electrode was prepared by attaching a mixture of the active material (84 wt.%), acetylene black (AB; 8 wt.%) as the conductive additive and polytetrafluoroethylene (PTFE; 8 wt.%) as the binder to an aluminum mesh. The total mass of the active material per electrode was about 7–8 mg. Throughout the present study, the electrochemical capacity was expressed in terms of per initial mass of  $\text{Li}_2\text{MnO}_3$ . The electrode was tested in an IEC R2032 coin-type cell assembled with a sodium or lithium foil counter electrode, a separator (Celgard 2400) and the electrolyte ( $1 \text{ mol} \cdot \text{L}^{-1}$  of  $\text{LiPF}_6$  or  $\text{NaPF}_6$  in ethylene carbonate/diethylene carbonate, EC/DEC (1:1 volume ratio)). On initial sodiation process, the cell was galvanostatically discharged (*i.e.*, Na inserted or sodiated) at the current density of  $10 \text{ mA} \cdot \text{g}^{-1}$ , until the potential reached 1.5 V vs.  $\text{Na}^+/\text{Na}$ , at which it was then potentiostatically discharged until the current density dropped to  $1 \text{ mA} \cdot \text{g}^{-1}$ . Following process, the cell was galvanostatically charged and discharged at the current density of  $10 \text{ mA} \cdot \text{g}^{-1}$ . The electrochemical properties of the electrodes were evaluated using a battery testing system (BLS series, Keisokuki Center).

### 2.3. Material characterization

The crystallographic structures of the samples were characterized by a laboratory X-ray diffractometer (XRD, Rigaku RINT Cu  $K\alpha$ ) and by synchrotron radiation XRD (SR-XRD, SPring-8, BL19B2). For the SR-XRD, the samples were placed in a glass capillary with a 0.5 mm outer diameter. The data were collected using a Debye-Scherrer camera with an imaging plate. The wavelength of the X-ray was calibrated to  $\lambda/\text{nm} = 0.06995$  using  $\text{CeO}_2$  as the standard material. The diffraction angle,  $2\theta$ , ranged from  $5.00$  to  $78.00^\circ$ , for

which one scan took 300 s. The precise crystallographic structures of the samples were determined by the Rietveld refinements of the SR-XRD data using the RIETAN-FP program [14].

The molar ratio of Na to Mn ( $\text{Na}/\text{Mn}$ ) was evaluated by an inductively-coupled plasma (ICP) analysis. The local structure and valence shift of the Mn ion were evaluated by X-ray absorption spectroscopy (XAS, Rits, BL3). The morphology of the sample powders was observed using a scanning electron microscope (SEM, JSM-6390 JEOL) and the distribution of the constituent elements was detected by energy dispersive X-ray spectroscopy (EDS). The nano structure of the sample powders was observed using a transmission electron microscope (TEM, 3000F, JEOL) equipped with an electron energy-loss spectrometer (EELS), by which the chemical state of the elements was measured.

## 3. Results and discussion

### 3.1. Precursor $\text{Li}_2\text{MnO}_3$

The XRD profile of the precursor, Fig. 1, is quite consistent with that simulated for the monoclinic  $\text{Li}_2\text{MnO}_3$  phase (PDF #01-084-1634, space group  $C2/m$ ). The profile is free of impurity signals, evidence for a successful synthesis. One finds from the SEM image inset in Fig. 1 that the  $\text{Li}_2\text{MnO}_3$  sample is comprised of a mixture of spherical and hexagonal particles of  $\sim 300 \text{ nm}$  diameter.

### 3.2. Sodiation of $\text{Li}_{2-x}\text{MnO}_3$

Fig. 2 shows the electrochemical potential profiles during the initial charge (*i.e.*, delithiation) process of the  $\text{Li}_2\text{MnO}_3/\text{Li}$  cell and during the subsequent discharge (*i.e.*, sodiation) of the  $\text{Li}_{2-x}\text{MnO}_3/\text{Na}$  cell. This result is compared to that during the discharge process of the  $\text{Li}_{2-x}\text{MnO}_3/\text{Li}$  cell (*i.e.*, lithiation). The lower abscissa indicates the electrochemical capacity in terms of  $\text{mA} \cdot \text{h} \cdot \text{g}^{-1}$  and the upper one is converted to the molar equivalent (mol eq) of Li or Na in the  $\text{Li}_{2-x}\text{MnO}_3$  by assuming that the observed capacity would purely result from the alkali metal extraction and insertion; namely,  $460 \text{ mA} \cdot \text{h} \cdot \text{g}^{-1}$  corresponds to 2.0 mol eq. The left hand-side ordinate indicates the potential difference referenced to Li metal and the right hand-side one to Na metal, in which the numerals of the latter are shifted +0.3 from the former in order to reflect the difference in the standard redox potentials of these metals; *i.e.*,  $-3.0$  and  $-2.7 \text{ V}$  vs. NHE for Li and Na, respectively. During the initial delithiation, a potential plateau is observed at around 4.5 V vs.  $\text{Li}^+/\text{Li}$  which corresponds to the oxygen release [12]. When the charge capacity of  $\text{Li}_2\text{MnO}_3$  reaches  $460 \text{ mA} \cdot \text{h} \cdot \text{g}^{-1}$ ,

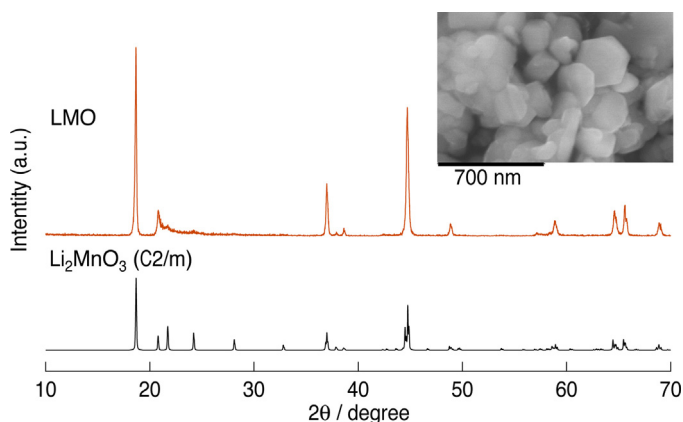
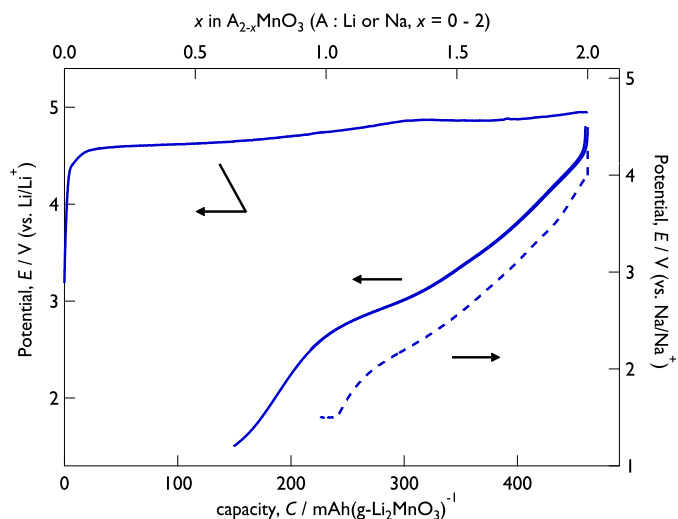


Fig. 1. XRD profile and a SEM image of the as-prepared  $\text{Li}_2\text{MnO}_3$  precursor. (X-ray: Cu  $K\alpha$ )



**Fig. 2.** Electrochemical potential profiles of the  $\text{Li}_2\text{MnO}_3$  electrode during the initial delithiation (solid line) and the subsequent sodiation (dashed line) or lithiation (solid line).

the electrode potential rises to 4.9 V vs.  $\text{Li}^+/\text{Li}$ . During the subsequent sodiation,  $\text{Li}_{2-x}\text{MnO}_3$  is capable of inserting 0.99 mol eq of Na ions (or  $238 \text{ mA} \cdot \text{h} \cdot \text{g}^{-1}$ ). The fact that the capacity of the lithiation exceeds that of the sodiation and the potential of the former is higher than that of the latter even if taking into account the 0.3 V difference in the redox potentials of Li and Na implies that  $\text{Li}^+$  is more easily inserted into  $\text{Li}_{2-x}\text{MnO}_3$  than  $\text{Na}^+$ , probably due to the smaller ionic radius of the former (0.076 nm) than the latter (0.102 nm).

The ICP measurement suggests that 0.96 mol eq of Na is contained in the sodiated  $\text{Li}_{2-x}\text{MnO}_3$ , which is consistent with the electrochemical capacity observed during the sodiation. However, the ICP measurement also detected 0.2–0.4 mol eq of Li residing in the  $\text{Li}_{2-x}\text{MnO}_3$  both before and after the sodiation (i.e.,  $x = 1.6 - 1.8$ ), which is at odds with the initial delithiation capacity. We suspect that certain side reactions, such as the decomposition of the electrolyte at a higher potential, may be involved in the initial delithiation process. The residual Li-containing phase is also detected by TEM and SR-XRD as shown below.

As for the structure of the sodiated  $\text{Li}_{2-x}\text{MnO}_3$ , see the “TEM and EELS observation” and its subsequent sections.

### 3.3. Electrode performance

Fig. 3 compares the charge and discharge profiles of the cells,  $\text{Li}_{2-x}\text{MnO}_3/\text{Li}$  (LMO) and  $\text{Li}_{2-x}\text{MnO}_3/\text{Na}$  (NMO). Initially, the reversible capacity of the LMO exceeds that of the NMO. However, after more than 30 cycles, the capacity of the NMO surpasses that of the LMO. The slope of the charge and discharge profiles of the LMO becomes steeper than that of the NMO upon cycling, especially above 3.5 V vs.  $\text{Li}^+/\text{Li}$  or 3.2 V vs.  $\text{Na}^+/\text{Na}$ , implying more serious damage in the LMO than in the NMO.

The cycle trends in the discharge capacity of the LMO and NMO are compared in Fig. 4. The potential range of the cycle test was set to 2.5–4.5 V vs.  $\text{Li}^+/\text{Li}$  for the LMO and 1.5–4.2 V vs.  $\text{Na}^+/\text{Na}$  for the NMO, so that the first discharge capacities of both the LMO and NMO are around  $250 \text{ mA} \cdot \text{h} \cdot \text{g}^{-1}$ . Although the LMO enjoys a higher capacity than the NMO during the initial ten cycles, its capacity significantly decays to less than  $100 \text{ mA} \cdot \text{h} \cdot \text{g}^{-1}$  in the following ten cycles. On the other hand, the NMO retains about 85% of the second discharge capacity observed during the second cycle after 50 cycles, i.e.,  $160 \text{ mA} \cdot \text{h} \cdot \text{g}^{-1}$ .

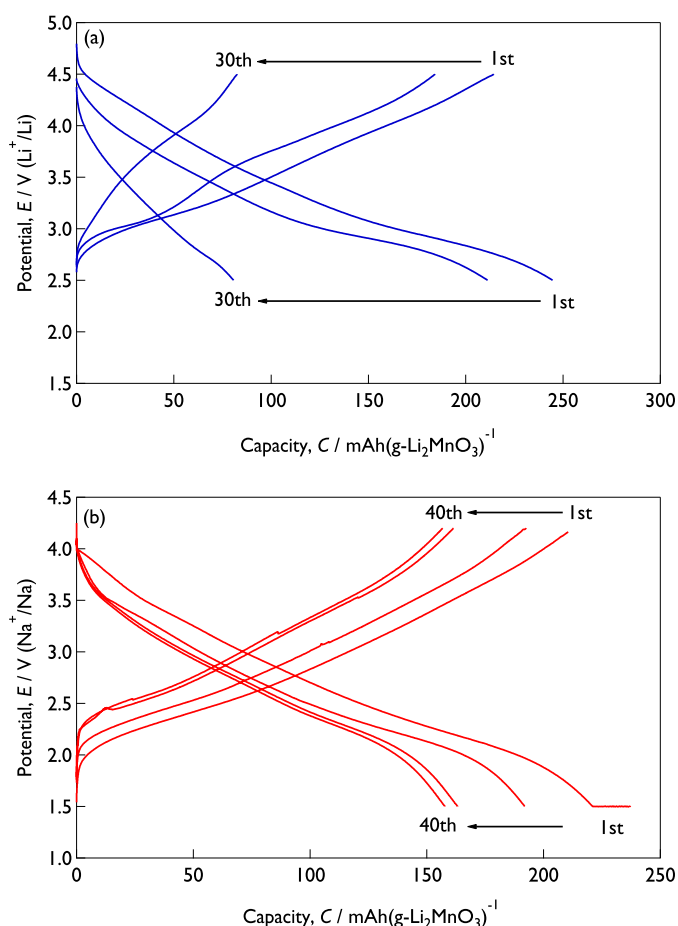


**Fig. 3.** Charge and discharge profiles of the  $\text{Li}_{2-x}\text{MnO}_3$ -electrodes versus (a) Li (LMO) and (b) Na (NMO).

The coulombic efficiency of the NMO maintains more than 98–99% after a few initial cycles, while that of the LMO drops to less than 90%. This suggests that the large structural distortion due to the Mn migration during the cycling is severer for Li insertion and extraction than for Na.

### 3.4. TEM and EELS analyses

Fig. 5 shows the TEM images of (a) as-prepared  $\text{Li}_2\text{MnO}_3$ , (b)  $\text{Li}_{2-x}\text{MnO}_3$  and (c) sodiated  $\text{Li}_{2-x}\text{MnO}_3$ . The high crystallinity of the

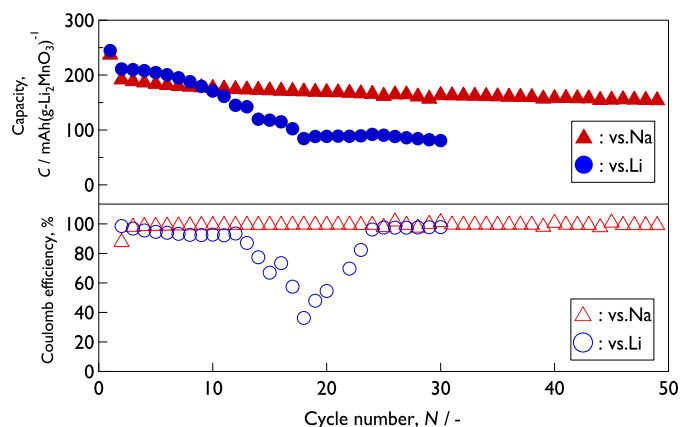


**Fig. 4.** Cycle trends in the discharge capacity of the  $\text{Li}_{2-x}\text{MnO}_3$ -electrodes using Li (LMO) and Na (NMO) as the counter electrode.

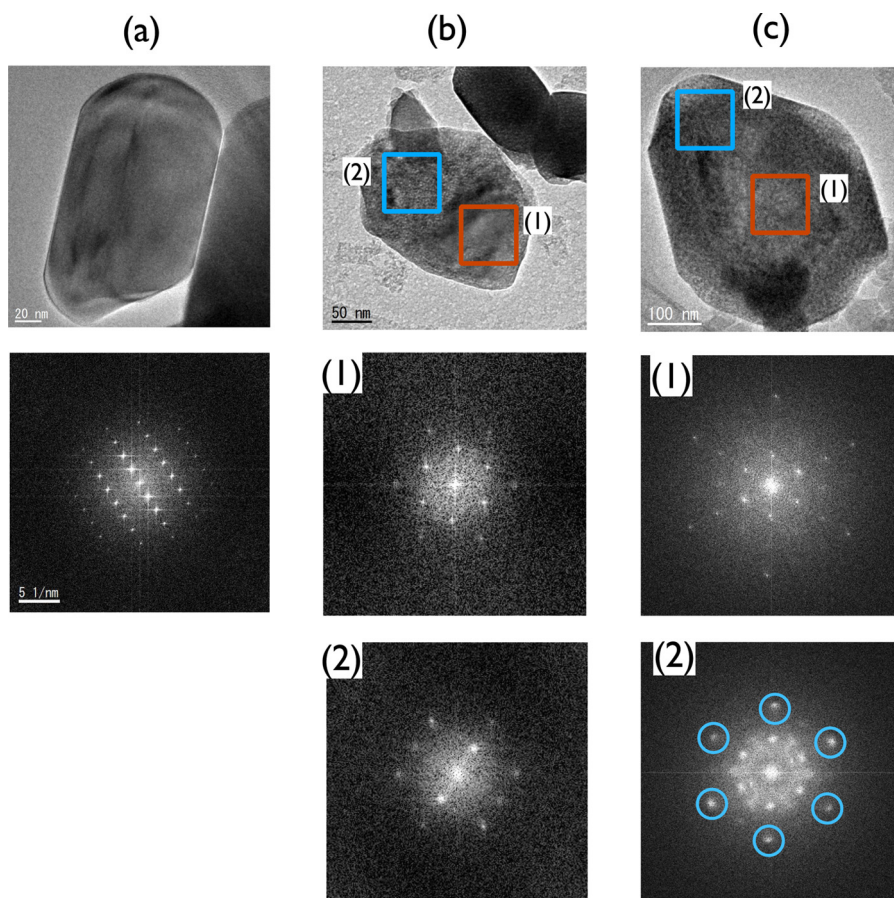


**Fig. 5.** TEM observation of (a) as-prepared  $\text{Li}_2\text{MnO}_3$ , (b)  $\text{Li}_{2-x}\text{MnO}_3$  and (c) sodiated  $\text{Li}_{2-x}\text{MnO}_3$ . Top: real-space images, Middle: diffraction patterns from a domain in which residual Li was observed after delithiation and Bottom: diffraction patterns from a domain which was completely delithiated.

as-prepared  $\text{Li}_2\text{MnO}_3$  is reflected in its fine diffraction spots, which are well assigned to the space group  $C2/m$ , consistent with Fig. 1. In the particles after the delithiation,  $\text{Li}_{2-x}\text{MnO}_3$ , Fig. 5(b), we found two domains distinguishable by their diffraction patterns, one of which is attributable to the zone axis  $[112]$  of the spinel structure (space group  $Fd\bar{3}m$ , Fig. 5(b-1), and the other to  $[001]$  of  $C2/m$ , Fig. 5(b-2). The spinel domain should be the unreacted  $\text{Li}_2\text{MnO}_3$  since the inter-planar spacing calculated from the diffraction spots coincides with that from the electron diffraction simulated from the structural model of  $\text{Li}_2\text{MnO}_3$  [15]. The  $Fd\bar{3}m$  domain is considered to be the reacted (i.e., delithiated) phase which has a spinel structure, i.e.,  $\lambda\text{-MnO}_2$ .

The presence of the Li residue is consistent with the ICP measurement mentioned in the section “Sodiation of  $\text{Li}_{2-x}\text{MnO}_3$ ”. The arrangement of the oxygen atoms in the  $[112]$  plane of  $Fd\bar{3}m$  resembles that in the  $[001]$  plane of  $C2/m$ , suggesting that the interface between these two phases is coherent [16].

After the sodiation, Fig. 5(c), while the unreacted  $C2/m$  phase retains its space group and lattice constant intact, the diffraction spots from the  $Fd\bar{3}m$  domain significantly change. The following detailed analysis leads to the conclusion that this sodiated domain is not a layered structure, but remains to be a spinel structure, although it may be tetragonally distorted. The six diffraction spots marked with circles in Fig. 5(c-2) nearly form a regular hexagon, giving the inter-planar distance ( $d$ -spacing) of 0.149–0.152 nm. Were the sodiated domain the layered structure of  $C2/m$  space group, i.e., layered  $\alpha\text{-NaMnO}_2$ , Fig. 5(c-2) should be along the zone axis  $[001]$  and the six spots should correspond to the Miller indices of  $\pm 2 \pm 2 0$  and  $\pm 4 0 0$ , respectively. However, the experimentally observed  $d$ -spacing of layered  $\alpha\text{-NaMnO}_2$  of these planes is 0.13 nm

[22], which is inconsistent with the present result. In other words, in order for the corresponding  $d$ -spacing of the layered structure to be 0.149–0.152 nm, the Mn–O distance should be 0.22–0.26 nm, which is unlikely long by considering their Shannon radii. Another possibility is that the sodiated domain remains to be a spinel. If the six spots precisely form a regular hexagon, the phase is a cubic spinel (e.g.,  $Fd\bar{3}m$ ), while if it is irregular, the phase is considered tetragonally distorted (e.g.,  $I4_1/amd$ ). The blur spots, however, do not allow us to decisively state that the 3% difference between 0.149 and 0.152 nm is significant. We proceed the analysis by adopting the lower-symmetry space group of  $I4_1/amd$ , which is consistent with the Jahn–Teller distortion of Mn(III). In this interpretation, Fig. 5(c-2) is considered along the zone axis  $[201]$  of  $I4_1/amd$  and the Miller indices of the six spots correspond to  $040$ ,  $0\bar{4}0$ ,  $2\bar{2}4$ ,  $2\bar{2}\bar{4}$ ,  $224$  and  $22\bar{4}$  respectively, yielding the lattice constants  $a/\text{nm}=0.595$  and  $c/\text{nm}=0.8671$ . Incidentally, the 3% of distortion of the present material, if any, is smaller than that of  $\text{Li}_2\text{Mn}_2\text{O}_4$  (7%), for which we suspect the reason is that the defects in the Mn site observed by EELS below absorb the Jahn–Teller distortion. By the sodiation, the lattice of the spinel phase expands by 18% in the volume which is much larger than that of other Na inserting materials with layered structures [17]. Therefore, we consider that the spinel to layer transition of  $\lambda\text{-MnO}_2$  has not occurred during sodiation in this study.

Fig. 6 shows the electron energy loss spectra (EELS) of (a) the delithiated (reacted) domain in  $\text{Li}_{2-x}\text{MnO}_3$  and (b) the sodiated domain after the sodiation of  $\text{Li}_{2-x}\text{MnO}_3$ . The spectra from the unreacted Li-residing domains (not shown) were used as a reference of  $\text{Li}_2\text{MnO}_3$ . The binding energy of the Na  $L$ -edge, ca. 38 eV, is reflected in the increase in the shoulder over the background after the sodiation. A small peak at around ca. 38 eV in Fig. 6(b), which corresponds



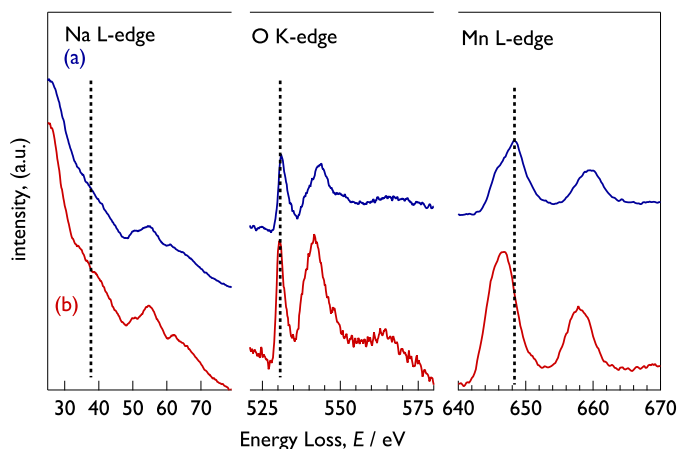


**Fig. 6.** EELS spectra of (a) delithiated domain in  $\text{Li}_{2-x}\text{MnO}_3$  and (b) sodiated domain after sodiation of  $\text{Li}_{2-x}\text{MnO}_3$ .

to the binding energy of the Li L-edge, may imply the presence of Li in the sodiated domain as well. However, EELS detects the signal from several tens nanometers region, so that the profile may contain the signal from the unreacted  $\text{Li}_2\text{MnO}_3$  domain. While no shift was observed in the oxygen K-edge, the manganese L-edge shifted to a lower binding energy after the sodiation, reflecting the reduction of  $\text{Mn}^{4+}$  to  $\text{Mn}^{3+}$  as in reaction (2).

The molar ratios of oxygen to manganese (O/Mn) was semi-quantitatively evaluated by comparing the peak areas of the O K-edge and Mn L-edge for each of which the integration ranges were from 550 to 555 eV and from 635 to 670 eV, respectively. To cancel out the intensity drift, the two signals (O K and Mn L) were simultaneously recorded. Normalizing the peak area ratio observed in the unreacted  $\text{Li}_2\text{MnO}_3$  domain to 3.0, we found O/Mn to be 2.4–2.5 in the delithiated domain of  $\text{Li}_{2-x}\text{MnO}_3$ ; i.e., the initial delithiation is accompanied by 0.5–0.6 mol eq of the release oxygen (cf. the reaction (1)) [16].

The O/Mn ratio after sodiation is 2.5–2.7 in the reacted domain, which barely shifted from that before the sodiation. The oxygen uptake reported by Tabuchi *et al.* [21] during the lithiation of  $\text{Li}_{1+x}(\text{Fe}_{0.25}\text{Mn}_{0.75})\text{O}_2$  was not observed<sup>1</sup>. The fact that O/Mn ratio exceeds 2.0 suggests the Mn sites in the reacting domain abound in defects. These Mn defects might have prohibited the spinel phase from returning to the layered structure in contrast to what is observed by Yabuuchi *et al.* [23] in which a partial transition from spinel to layer is reported in a Na cell using  $\text{LiMn}_2\text{O}_4$ .

### 3.5. Synchrotron XRD

The crystallographic change before and after the sodiation was investigated using *ex-situ* SR-XRD. Fig. 7 shows the SR-XRD patterns of (a) as-prepared  $\text{Li}_2\text{MnO}_3$ , (b) delithiated  $\text{Li}_{2-x}\text{MnO}_3$  and (c) sodiated  $\text{Li}_{2-x}\text{MnO}_3$ . The initial sharp peaks of the as-prepared  $\text{Li}_2\text{MnO}_3$  belong to the  $C2/m$  transitions to the  $Fd\bar{3}m$  spinel structure, so called  $\lambda$ - $\text{MnO}_2$ , with a slight broadening of the peaks after the delithiation. The peak broadening would ascribed to the structural distortion of  $\lambda$ - $\text{MnO}_2$  since the O/Mn ratio of  $\text{Li}_{2-x}\text{MnO}_3$  is estimated to be more than 2.0 indicating that there has some defects in the Mn site of  $\lambda$ - $\text{MnO}_2$  structure. One also notices that a small amount of unreacted  $\text{Li}_2\text{MnO}_3$  remains after the delithiation.

These results agree with our TEM observation. Yan *et al.* observe a gradual structural change from  $C2/m$  to  $Fd\bar{3}m$  during the lithium

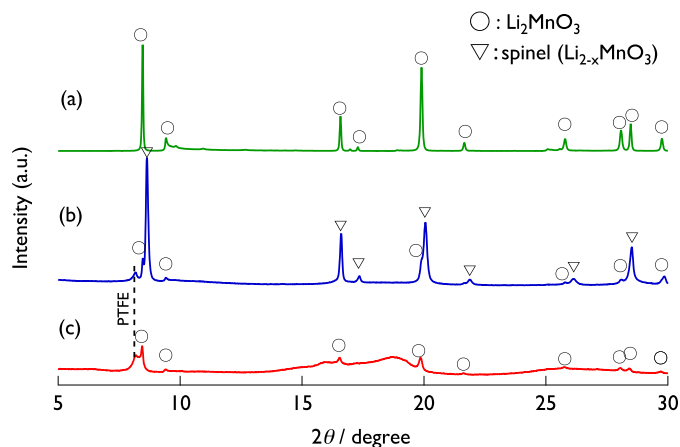


**Fig. 7.** SR-XRD patterns of (a) as-prepared  $\text{Li}_2\text{MnO}_3$ , (b) delithiated  $\text{Li}_{2-x}\text{MnO}_3$  and (c) sodiated  $\text{Li}_{2-x}\text{MnO}_3$ . ( $\lambda/\text{nm} = 0.06995$ )

extraction and insertion cycling of  $\text{LiMnO}_2$  [16], which is in contrast to our result of one-step transition to  $Fd\bar{3}m$  through the Li extraction. We speculate that the greater amount of Li extraction during the first charge process in our study than Yan's (i.e., 460 vs. about  $100 \text{ mA} \cdot \text{h} \cdot \text{g}^{-1}$ ) invokes the more drastical phase change in the former than in the latter.

No peak shift was observed between the as-prepared  $\text{Li}_2\text{MnO}_3$  and the unreacted  $\text{Li}_2\text{MnO}_3$  domain of  $\text{Li}_{2-x}\text{MnO}_3$ , suggesting that the delithiation is biphasic as Yu *et al.* reported [11]. The mass fraction of the unreacted  $\text{Li}_2\text{MnO}_3$  phase in  $\text{Li}_{2-x}\text{MnO}_3$  is evaluated to be about 30 wt.% by the Rietveld refinement of the SR-XRD profile. Assuming the spinel phase to be  $\text{MnO}_2$ , one finds from this mass fraction that the molar ratio of Li to Mn in the entire delithiated sample to be 0.38, which is in good agreement with the ICP measurement ( $\text{Li} / \text{Mn} = 0.45$ ).

After the sodiation of  $\text{Li}_{2-x}\text{MnO}_3$ , very broad humps show up, with the unreacted  $\text{Li}_2\text{MnO}_3$  phase remaining. The TEM diffraction spots from the reacted domain (Fig. 5(c)) suggest that the humps stem from the completely sodiated phase,  $\text{NaMnO}_2$ , having the spinel structure, yet its crystalline periodicity is considerably lost. In general, the crystallite size is estimated from the peak widths of the XRD based on the Scherrer equation. However, the humps in Fig. 7(c) are so broad that the equation does not exactly apply.

We then directly calculated in the real spaces from the diffraction profile of one crystallite particle without any periodic condition as follows. The intensity,  $I$ , of the X-ray (wavelength =  $\lambda$ ) diffracted at the angle  $\theta$  from the atoms situated at  $\vec{r}_i$  and  $\vec{r}_j$  is:

$$|I(\theta)|^2 \propto \sum_i \sum_{j>i} f_j(\theta) \exp \{ 2\pi i \vec{K} \cdot (\vec{r}_j - \vec{r}_i) \} \quad (3)$$

where  $f_j$  is the atomic scattering factor of the atom  $j$ , and  $\vec{K}$  is the scattering vector of which the magnitude is:

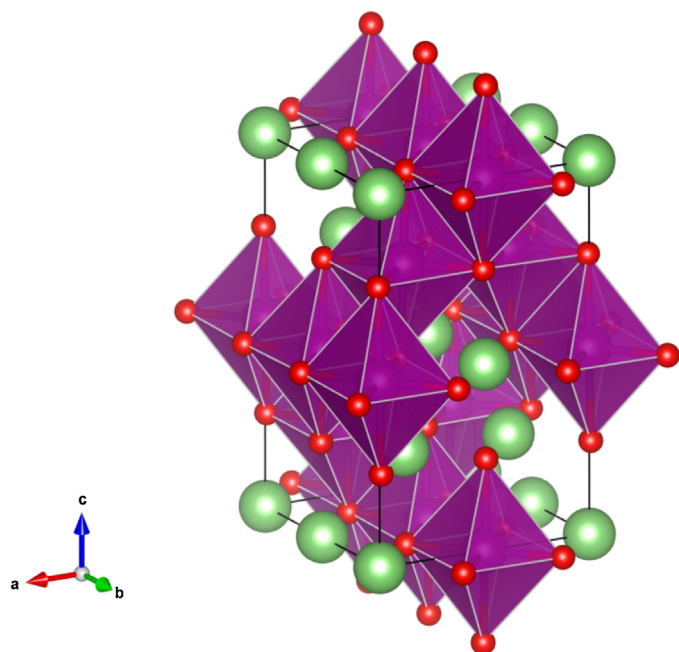
$$|\vec{K}| = \frac{2 \sin \theta}{\lambda}. \quad (4)$$

Fig. 9 shows the simulated pattern in which superimposed are two profiles of the spinel  $\text{NaMnO}_2$  with 0.4 and 1.6 nm sizes, or several unit cells. The structure model is given in Fig. 8 and Table 1 with the lattice constant  $a/\text{nm} = 0.595$  and  $c/\text{nm} = 0.8671$  based on the TEM diffraction described above.

Note that we don't consider the presence of the Li ion in the structure.

The coordinates of the oxygen atom are fixed based on the EXAFS result (see the next section). The simulated profile well reproduces the experimental result. The delithiated domain of  $\text{Li}_{2-x}\text{MnO}_3$  retains its spinel structure after sodiation, but loses its crystallinity

<sup>1</sup> Strictly speaking, this result stipulates that the chemical formula of  $\text{Li}_{2-x}\text{MnO}_3$  be written as " $\text{Li}_{2-x}\text{MnO}_y$  where  $y = 2.4 \sim 2.6$ ", etc., which we avoid for simplicity.



**Fig. 8.** Crystallographic structure model of spinel  $\text{NaMnO}_2$  ( $I4_1/amd$ ) to simulate the SR-XRD profile in Fig. 9.

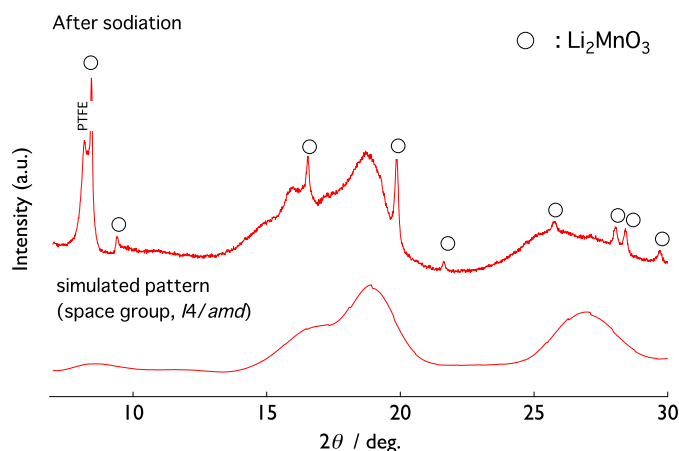


**Fig. 9.** XRD pattern of sodiated  $\text{Li}_{2-x}\text{MnO}_3$  and simulated pattern ( $I4_1/amd$ , superimposition of crystallites of 0.4 and 1.6 nm in size).

inasmuch as the regularity of only one or two unit cells remains, which nonetheless suffices to give spots in the TEM diffraction.

We confirmed that the XRD pattern of desodiated NMO remained to be a spinel type structure (see Fig. S1 in Supporting Information).

**Table 1**

Crystallographic structure model of spinel  $\text{NaMnO}_2$  ( $I4_1/amd$ ) to simulate the SR-XRD profile in Fig. 9. A possible partial occupation of Li in the Na site is not taken into account.

Atom	Wyckoff site	X	Coordinates Y	Z
Na	8c	0	0	0
Mn	8d	0.0	0.0	1/2
O	16h	0.0	0.487	0.252

The model is not consider the presence of Li and the site occupancy of each element.

### 3.6. X-ray absorption spectroscopy (XAS)

Figs. 10(b) and (c) show the XANES and EXAFS spectra of the Mn K-edge, respectively, taken at the states indicated by the numbers 1–4 in the potential profile, Fig. 10(a). Each state corresponds to (1) as-prepared  $\text{Li}_2\text{MnO}_3$ , (2) delithiated  $\text{Li}_{2-x}\text{MnO}_3$ , (3) sodiated  $\text{Li}_{2-x}\text{MnO}_3$ , i.e., NMO and (4) desodiated NMO. The inset in (b) magnifies the pre-edge region, 6530–6546 eV, which reflects the  $1s \rightarrow 3d$  transition. The pre-edge signal of the reduced sample, (3), is observed at (B) 6537 eV, which is lower than the other oxidized samples, i.e., (1), (2) and (3) at (A) 6539 eV. In the case of lithium manganese oxide in general, the shift to the lower binding energy of the Mn pre-edge indicates the reduction of Mn(IV) to Mn(III), which

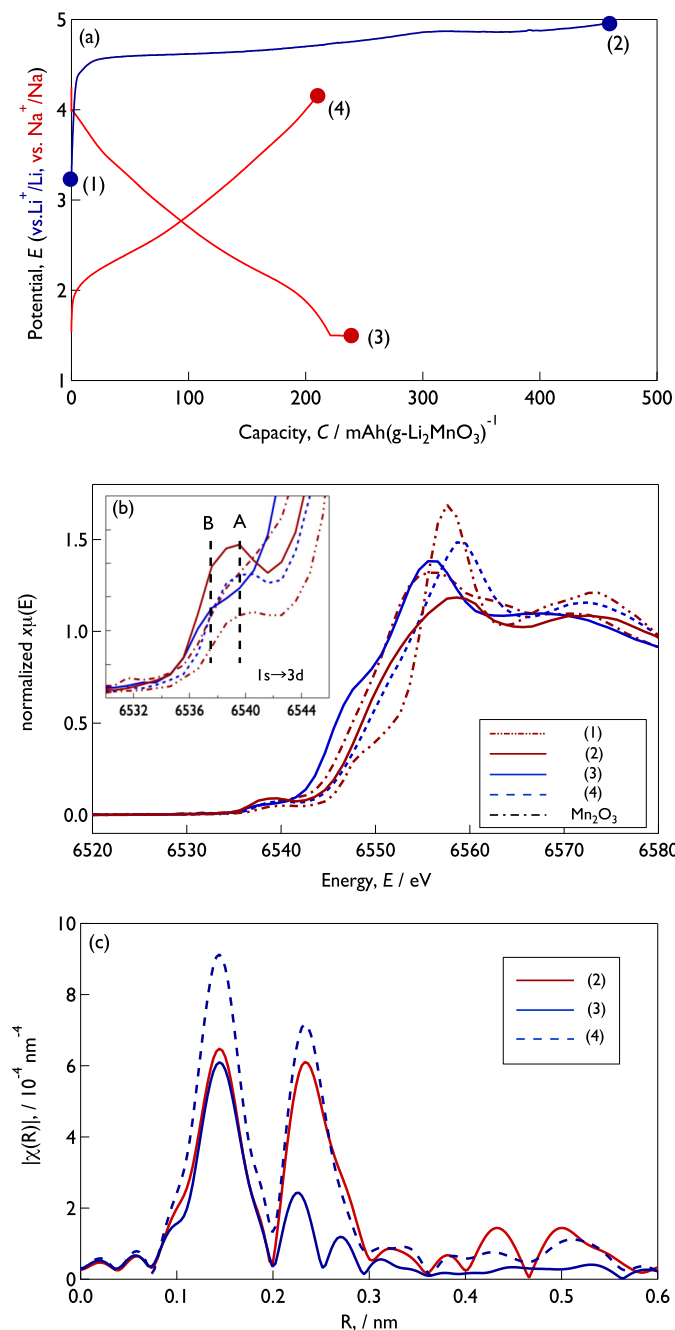


**Fig. 10.** (a) Potential profiles of the initial delithiation and subsequent sodiation and desodiation. Numbers 1–4 indicate the states in which the (b) XANES and (c) EXAFS spectra of the Mn K-edge were taken.

distorts the initially centro-symmetric  $\text{MnO}_6$  octahedron due to the Jahn–Teller effect [18,19]. In the present material, the sodiation triggers a similar distortion in the structure, resulting in the broad humps in the SR-XRD profile.

Fig 10(c) shows the radial correlation,  $\chi$ , as a function of the distance from Mn,  $R$ , derived from the EXAFS spectra taken at points (2), (3) and (4) in Fig 10(a). The first peak in  $\chi$  centering at  $R/\text{nm} = 0.15$  is attributed to the Mn–O distance. The peak shape does not apparently change after sodiation. The distortion in the  $\text{MnO}_6$  octahedron after the sodiation inferred from the XANES spectrum may be too subtle to be reflected in the peak shape of  $\chi^2$ . The second peak in  $\chi$  at  $R/\text{nm} = 0.2\text{--}0.3$  corresponds to the Mn–Mn distance. The intensity of this peak significantly decreases during the sodiation, suggesting a significant loss in the crystallographic regularity. This observation is also consistent with the analysis described in the section “SR-XRD”. The Mn–Mn peak intensity increases when the sodiated sample is desodiated again, implying that the regularity is reinstated to some extent.

### 3.7. Structural change and cycle-life stability

When  $\text{Li}_{2-x}\text{MnO}_3$  is cycled in the Li-system, its structure shuttles between the spinel- and layer-type. During this transition, Mn is prone to migrate from the initial octahedral site to the tetrahedral site, which clogs the Li diffusion in the electrode, resulting in the poor cycle-stability [9]. On the other hand, the present study proved that  $\text{Li}_{2-x}\text{MnO}_3$  retains the spinel structure in the Na-system, although its crystallographic regularity is significantly lost when sodiated. In case of  $\text{AMnO}_2$ , the layer structure is retained during the redox reaction when  $A = \text{Na}$ , resulting in a good cycle stability [5], whereas a quick degradation is observed when  $A = \text{Li}$  [20]. Whether the spinel- or layer-structure, the poor stability results from the Mn-migration triggered by the structural phase transition. A computational study by Reed *et al.* indeed suggests that the Mn-migration to the tetrahedral sites is energetically unfavorable compared to the Li counterpart due to the difference in the ionic sizes [10]. The better cycle stability of  $\text{Li}_{2-x}\text{MnO}_3$  in Na than in Li is presumably achieved by preventing the Mn-migration.

## 4. Conclusion

A spinel manganese oxide,  $\text{Li}_{2-x}\text{MnO}_3$ , was synthesized by electrochemically extracting Li from  $\text{Li}_2\text{MnO}_3$ , intending to use it as a positive electrode material for the Na-ion battery. The initial discharge capacity of  $\text{Li}_{2-x}\text{MnO}_3$  exceeded  $230 \text{ mA} \cdot \text{h} \cdot \text{g}^{-1}$ , corresponding to more than 1.0 moleq of Na insertion. The discharge capacity remained more than 80% of that observed for the second cycle after 50 cycles. This cycle-stability is superior to the case when  $\text{Li}_{2-x}\text{MnO}_3$  was used in the Li-system. The TEM observation and SR-XRD analysis revealed that the material retained its initial spinel structure during the sodiation and desodiation, although the crystallographic regularity was significantly lost during the sodiation. Whether the structural phase transition takes place or not during the redox reaction can be a key for the long cycle-life.

## Acknowledgement

We thank Dr. Masaki Katayama for helping us with the XAS experiment and for his valuable comments. This study was financially supported by JSPS Kakenhi Grant #26889074.

## Appendix A. Supplementary Data

Supplementary data associated with this article can be found, in the online version, at <http://dx.doi.org/10.1016/j.electacta.2016.07.038>.

## References

- [1] S. Komaba, W. Murata, T. Ishikawa, N. Yabuuchi, T. Ozeki, T. Nakayama, A. Ogata, K. Gotoh, K. Fujiwara, Electrochemical Na Insertion and Solid Electrolyte Interphase for Hard-Carbon Electrodes and Application to Na-Ion Batteries, *Advanced Functional Materials* 21 (20) (2011) 3859.
- [2] C. Delmas, J.-J. Braconnier, C. Fouassier, P. Hagenmuller, Electrochemical intercalation of sodium in  $\text{Na}_x\text{CoO}_2$  bronzes, *Solid State Ionics* 4 (1981) 165.
- [3] J.-J. Braconnier, C. Delmas, P. Hagenmuller, Etude par Desintercalation electrochimique des systemes  $\text{Na}_x\text{CrO}_2$  et  $\text{Na}_x\text{NiO}_2$ , *Materials Research Bulletin* 17 (c) (1982) 993.
- [4] A. Maazaz, C. Delmas, P. Hagenmuller, A study of the  $\text{Na}_x\text{TiO}_2$  system by electrochemical deintercalation, *Journal of inclusion phenomena* 1 (1) (1983) 45.
- [5] X. Ma, H. Chen, G. Ceder, Electrochemical Properties of Monoclinic  $\text{NaMnO}_2$ , *Journal of The Electrochemical Society* 158 (12) (2011) A1307.
- [6] A. Caballero, L. Hernán, J. Morales, L. Sánchez, J. Santos Peña, M.A.G. Aranda, Synthesis and characterization of high-temperature hexagonal  $\text{P2-Na}_{0.6}\text{MnO}_2$  and its electrochemical behaviour as cathode in sodium cells, *Journal of Materials Chemistry* 12 (4) (2002) 1142.
- [7] F. Sauvage, L. Laffont, J.-M. Tarascon, E. Baudrin, Study of the insertion/deinsertion mechanism of sodium into  $\text{Na}_{0.44}\text{MnO}_2$ , *Inorganic chemistry* 46 (8) (2007) 3289.
- [8] J. Reed, G. Ceder, Role of electronic structure in the susceptibility of metastable transition-metal oxide structures to transformation, *Chemical Reviews* 104 (10) (2004) 4513.
- [9] M.M. Thackeray, Manganese oxides for lithium batteries, *Progress in Solid State Chemistry* 25 (1997) 1.
- [10] J. Reed, G. Ceder, A. Van Der Ven, Layered-to-spinel phase transition in  $\text{Li}_x\text{MnO}_2$ , *Electrochemical and Solid-State Letters* 4 (6) (2001) A78.
- [11] D.Y. Yu, K. Yanagida, Y. Kato, H. Nakamura, Electrochemical activities in  $\text{Li}_2\text{MnO}_3$ , *Journal of The Electrochemical Society* 156 (2009) A417.
- [12] A.R. Armstrong, M. Holzapfel, P. Novák, C.S. Johnson, S.-H. Kang, M.M. Thackeray, P.G. Bruce, Demonstrating oxygen loss and associated structural reorganization in the lithium battery cathode  $\text{Li}[\text{Ni}_{0.2}\text{Li}_{0.2}\text{Mn}_{0.6}]\text{O}_2$ , *Journal of the American Chemical Society* 128 (26) (2006) 8694.
- [13] A. Armstrong, A. Robertson, P. Bruce, Overcharging manganese oxides: Extracting lithium beyond  $\text{Mn}^{4+}$ , *Journal of Power Sources* 146 (1–2) (2005) 275.
- [14] I. Fujio, M. Koichi, Three-dimensional visualization in powder diffraction, *Solid State Phenomena* 130 (2007) 15.
- [15] P. Strobel, B. Lambert-Andron, Crystallographic and magnetic structure of  $\text{Li}_2\text{MnO}_3$ , *Journal of Solid State Chemistry* 75 (1988) 90.
- [16] P. Yan, L. Xiao, J. Zheng, Y. Zhou, Y. He, X. Zu, S.X. Mao, J. Xiao, F. Gao, J.-G. Zhang, C.-M. Wang, Probing the degradation mechanism of  $\text{Li}_2\text{MnO}_3$  cathode for li-ion batteries, *Chemistry of Materials* 27 (2015) 975.
- [17] R. Kataoka, T. Mukai, A. Yoshizawa, T. Sakai, Development of high capacity cathode material for sodium ion batteries  $\text{Na}_{0.95}\text{Li}_{0.15}(\text{Ni}_{0.15}\text{Mn}_{0.55}\text{Co}_{0.1})\text{O}_2$ , *Journal of The Electrochemical Society* 160 (2013) A933.
- [18] A. Manceau, A.I. Gorshkov, V.A. Drits, Structural chemistry of Mn, Fe, Co and Ni in manganese hydrous oxides: Part 1. information from XANES spectroscopy, *American Mineralogist* 77 (1992) 1133.
- [19] C.R. Horne, U. Bergmann, M.M. Grush, R.C.C. Perera, D.L. Ederer, T.A. Callcott, E.J. Cairns, S.P. Cramer, Electronic structure of chemically-prepared  $\text{Li}_x\text{Mn}_2\text{O}_4$  determined by Mn x-ray absorption and emission spectroscopies, *The Journal of Physical Chemistry B* 104 (2000) 9587.
- [20] I. Davidson, R. McMillan, J. Murray, J. Greedan, Lithium-ion cell based on orthorhombic  $\text{LiMnO}_2$ , *Journal of Power Sources* 54 (1995) 232, proceedings of the Seventh International Meeting on Lithium Batteries.
- [21] M. Tabuchi, H. Kageyama, K. Kubota, H. Shibuya, K. Doumae, R. Kannno, Structural change during charge-discharge for iron substituted lithium manganese oxide, *Journal of Power Sources* 318 (2016) 18.
- [22] J. -Paul Parant, R. Olazcuaga, M. Devalette, C. Fouassier, P. Hagenmuller, Sur quelques nouvelles phases de formule  $\text{Na}_x\text{MnO}_2$  ( $x \leq 1$ ), *Journal of Solid State Chemistry* 3 (1971) 1.
- [23] N. Yabuuchi, M. Yano, S. Kuze, S. Komaba, Electrochemical behavior and structural change of spinel-type  $\text{Li}(\text{Li}_x\text{Mn}_{2-x})\text{O}_4$  ( $x = 0$  and 0.2) in sodium cells, *Electrochimica Acta* 82 (2012) 296.

<sup>2</sup> One can fit the first peak in  $\chi$  with a distorted  $\text{MnO}_6$  octahedron; namely, 0.194 nm equatorial- and 0.217 nm axial-bonds. However, considering the quality of the fitting, we deemed the result as unreliable.